

Cite this: *Catal. Sci. Technol.*, 2025,
15, 2229Na-decorated binary spinel ferrite catalysts for the
hydrogenation of CO₂ to olefins†Hanjun Lu,^a Xia Li,^a Guangchao Li,^a ^{*b} Xinlin Hong ^{**a} and Shik Chi Edman Tsang^b

Spinel ferrite catalysts, recognized for their unique physicochemical properties, have been extensively employed in CO₂ hydrogenation reactions. However, the specific roles of different transition metals in Na-decorated spinel ferrite for CO₂ hydrogenation to olefins remain underexplored. In this study, we designed a series of Na-decorated binary spinel ferrites by varying the type of the secondary metals. We found that doping with zinc reduces the hydrogenation ability, which enhances olefin selectivity. Conversely, adding copper facilitates catalyst reduction through H₂-spillover, with the CuFe interface increasing alcohol products. CoFe₂O₄ demonstrated the highest activity and olefin yield. Additionally, CoFe₂O₄ was found to promote the formation of the carbide phase and enhance the activation and dissociation of hydrogen, significantly boosting catalytic performance. Our findings pave the way for developing Na-decorated spinel catalysts tailored for selective olefin synthesis, with important implications for improving the efficiency of CO₂ hydrogenation processes.

Received 13th January 2025,
Accepted 18th February 2025

DOI: 10.1039/d5cy00033e

rsc.li/catalysis

Introduction

The increasing concentration of CO₂ in the atmosphere is closely related to climate issues such as global warming.¹ From a sustainability standpoint, CO₂ is a readily available and cost-effective carbon-based resource.² As a result, substantial effort has been invested in developing efficient CO₂ capture and utilization systems.³ The direct hydrogenation of CO₂ into value-added chemicals has garnered considerable attention during the past decades.^{4–9} Among the various carbon cycle options, the catalytic hydrogenation of CO₂ to olefins, using inexpensive hydrogen derived from renewable energy sources, stands out a promising route.¹⁰ However, CO₂ hydrogenation typically results in the formation of C₁ products, presenting a significant challenge for controlled C–C coupling to produce C₂₊ olefins.¹¹ This challenge has driven the scientific community to focus on designing and developing more effective catalysts.

Fe-based catalysts are generally recognized as highly active and cost-effective in CO₂ hydrogenation to olefins, due to

their intrinsic activity in both the reverse water gas shift (RWGS) reaction and the Fischer–Tropsch synthesis (FTS) process.¹² It is widely accepted that Fe₃O₄ and Fe₅C₂ are the primary active phases responsible for the RWGS reaction and the FTS process, respectively. Recently, the addition of secondary metals such as Zn²⁺, Co²⁺, Fe²⁺, Cu²⁺, and Mg²⁺ to trivalent Fe (Fe³⁺) forming lattice Fe oxides with spinel structure has emerged as an innovative strategy for designing efficient catalysts to drive the CO₂ hydrogenation reaction.¹³ These catalysts possess unique composition and tunable properties that distinguish them significantly from conventional bulk Fe materials. For instance, Zhang *et al.* demonstrated that ZnFe₂O₄ catalyst can enable the RWGS through the *in situ* formation ZnO and the ultrahigh dispersion of FeO_x on the surface, enabling C–C coupling and olefins synthesis over FeC_x species.¹⁴ Similarly, Kim *et al.* synthesized the carbon nanotube-supported Na-promoted CoFe₂O₄ catalysts (Na–CoFe₂O₄/CNT), which can facilitate the formation of the bimetallic alloy carbide (Fe_{1–x}Co_x)₅C₂ phase, differing from the typical χ -Fe₅C₂ active sites found in Fe-based catalysts, and exhibiting high CO₂ conversion and light olefin selectivity.¹⁵ Cu is widely used as a reduction promoter and promotes CO₂ hydrogenation to alcohols while suppressing the RWGS reaction. Choi *et al.* used delafossite-CuFeO₂ as the catalyst precursor to synthesize CuFe catalyst, achieving high selectivity for liquid hydrocarbons (C₅₊) and extremely low selectivity for CH₄, attributed to rapid reduction and selective carburization to form the Hägg iron carbide (χ -Fe₅C₂).¹⁶ However, previous research on ferrite

^a College of Chemistry and Molecular Sciences, Wuhan University, Wuhan 430072, P. R. China. E-mail: hongxl@whu.edu.cn

^b Department of Applied Biology and Chemical Technology, The Hong Kong Polytechnic University, Hong Kong 999077, China.
E-mail: guangchao.li@polyu.edu.hk

† Electronic supplementary information (ESI) available: Additional catalytic activity, SEM images, and TPD profiles (PDF). See DOI: <https://doi.org/10.1039/d5cy00033e>



spinel has mainly focused on the specific spinel catalysts, and a systematic study of different binary spinel ferrites during CO₂ hydrogenation process remains largely unexplored.

In this work, we prepared Na-decorated transition metals (Zn, Cu, Co) spinel ferrite catalysts for CO₂ hydrogenation to olefins. We investigated the promoting effects of different transition metals with spinel structures using a series of characterization techniques. The NaZnFe catalyst enhances olefin selectivity through electronic interactions, while the CuFe interface in the NaCuFe catalyst increases the production of higher alcohol products. Notably, the NaCoFe catalyst exhibits the best catalytic performance, achieving a CO₂ conversion of 33.2% alongside 68.8% olefin selectivity under mild conditions of 320 °C, 1 MPa, and 3000 mL g_{cat}⁻¹ h⁻¹.

Results and discussion

Catalytic performance of Fe-based catalysts in CO₂ hydrogenation

Fig. 1 and Table S1† present the catalytic performance of Fe-based catalysts for CO₂ hydrogenation under reaction conditions of 320 °C, 1 MPa and 3000 mL g_{cat}⁻¹ h⁻¹. Prior to the incorporation of transition metals, the NaFe catalyst exhibits high selectivity toward olefins (74.8%) at a CO₂ conversion of 27.7% and a CO selectivity of 16.8%. The chain

growth factor was calculated, yielding an α value of 0.67 for the NaFe catalyst (Fig. S1†). Among the Na-modulated binary spinel ferrite catalysts, the NaZnFe catalyst exhibits similar CO₂ conversion rates and CO selectivity, but with an increase in methane production. The findings suggest that the ZnFe₂O₄ precursor does not significantly enhance Fe-based catalysts for olefin production. The NaCuFe catalyst demonstrates relatively low olefin selectivity (62.2%), while significantly improving alcohol selectivity. Given that CuFe-based catalysts are typically active in synthesizing higher alcohols, we speculate that CuFe₂O₄ catalyst can regulate the dissociation of CO by forming a Cu-Fe_xC_y interface,^{17,18} promoting the generation of alcohols. The phase separation between Cu and Fe species also results in a decrease in α value (0.64).¹⁹ It is worth noting that the CO₂ conversion rate increases to 33.2% and the CO selectivity decreases to 12.8% on the NaCoFe catalyst. This indicates that the existence of CoFe₂O₄ makes an evident contribution to the FTS rate, which will accelerate the consumption of CO intermediate species and further increase the CO₂ conversion. However, the increased CH₄ selectivity reflects the decrease in chain growth probabilities, which can be evidenced by the α value of 0.54 (Fig. 1c). After comparing the reaction performance of these catalysts, the NaCoFe catalyst emerges as the most effective. Consequently, we explored the effect of varying Co content on the NaCoFe catalyst's performance. With increasing Co content (Fig. 1d and S2†), CO₂ conversion

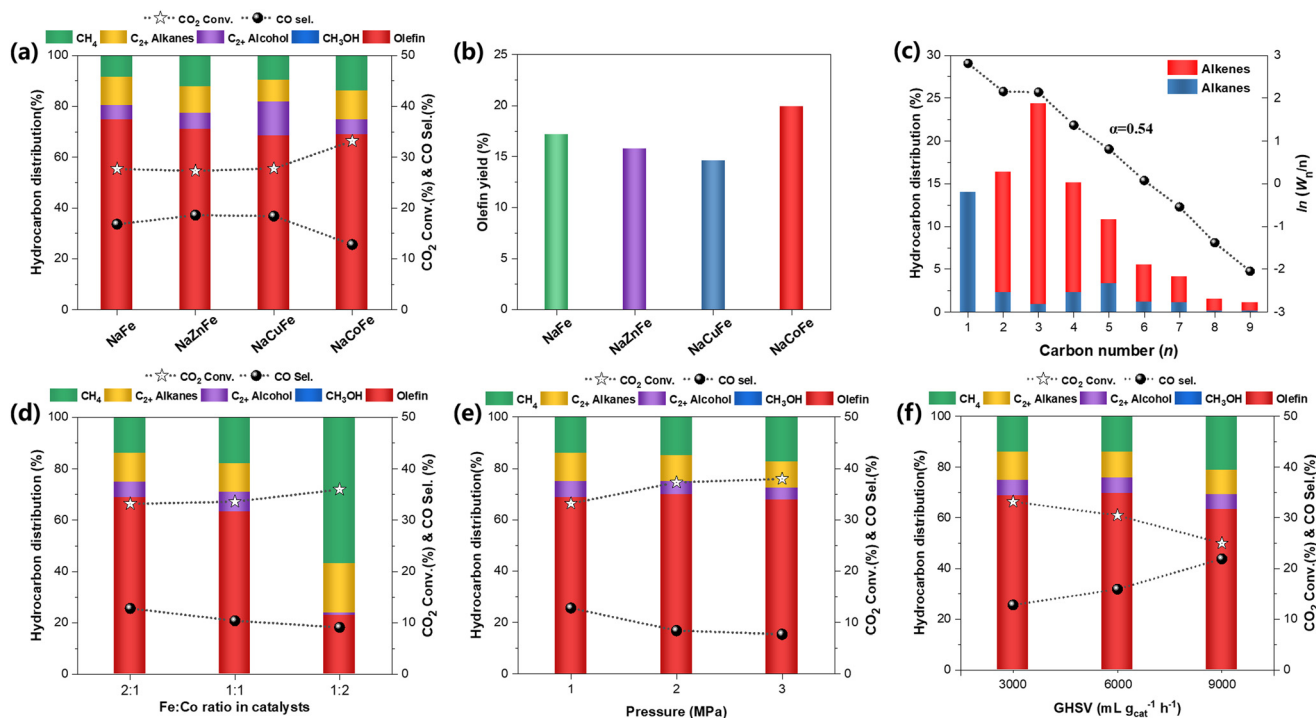


Fig. 1 Catalytic behaviors of CO₂ hydrogenation. (a) CO₂ conversion, CO selectivity, and CO-free selectivity for the organic product; (b) olefin yield over Fe-based catalysts. (c) the detailed alkane and olefin distribution, the ASF plot and the corresponding α value (α represents the probability of chain growth) over NaCoFe catalyst at 320 °C, 1 MPa, and 3 L g_{cat}⁻¹ h⁻¹; (d) effect of different Fe : Co molar ratio on the catalytic performance at 320 °C, 1 MPa, and 3 L g_{cat}⁻¹ h⁻¹; (e) effect of reaction pressure (1–3 MPa) on the catalytic performance at 320 °C, 3 L g_{cat}⁻¹ h⁻¹; (f) effect of gas hourly space velocity (GHSV) on the catalytic performance at 320 °C, 1 MPa.



gradually rises from 33.2 to 36.0%, and the CO selectivity decreases from 12.8 to 9.1%. Notably, the selectivity of undesirable CH_4 further increases, with the NaCoFe (1:2) catalyst yielding predominantly CH_4 at a selectivity of 56.8%, leading to a further decrease in the α value.

We further investigated the effect of different reaction conditions on the activity of the optimal NaCoFe catalyst. As the reaction pressure increases (Fig. 1e and S3[†]), the CO_2 conversion rate gradually increases while the CO selectivity decreases. Under a pressure of 3 MPa, the CO_2 conversion rate and CO selectivity reached 38.0% and 7.7%, respectively. Since the RWGS reaction is a gas volume invariant reaction, the amount of CO generated should be constant. The catalytic results indicate that high pressure promotes more CO molecules for subsequent conversion, thereby further promoting the conversion of CO_2 . We also tested the reaction performance at different temperatures and found that higher reaction temperatures improve both CO_2 conversion and olefin yield (Fig. S4[†]). This is because the RWGS reaction is endothermic while the hydrogenation reactions of CO are exothermic, thus, raising the temperature favors RWGS reaction, increasing the CO_2 conversion. As the reaction gas space velocity gradually increases (Fig. 1f and S5[†]), the CO_2 conversion rate of NaCoFe catalyst decreases, while its CO

selectivity increases. The shortened contact time can also lead to an increased selectivity for methane, as C-C coupling becomes more difficult, resulting in a decrease in olefin selectivity from 69.8% to 63.4%. As the GHSV increases from 3 to 9 $\text{L g}_{\text{cat}}^{-1} \text{h}^{-1}$, the olefin STY rises from 91 to 169 $\text{mg g}_{\text{cat}}^{-1} \text{h}^{-1}$. Despite the decrease in CO_2 conversion rate and increase in CO selectivity due to shortened contact time, the overall rate of olefin synthesis significantly improves due to the increased number of CO_2 and CO molecules participating in the reaction within the same timeframe. In summary, high temperature, high pressure, and low gas velocity are all beneficial for the conversion of CO_2 , thereby improving the catalytic activity for olefin synthesis.

Physicochemical properties of Fe based catalysts

The precursor of spinel structure was synthesized by an organic combustion method,²⁰ with Na modified catalysts prepared *via* impregnation. By controlling the impregnation process, the Na content in all catalysts was maintained at 2 wt%, and the molar ratio of Fe:M (M = Zn, Cu, or Co) was adjusted to closely match the stoichiometric ratio of spinel structure for the modified catalysts.

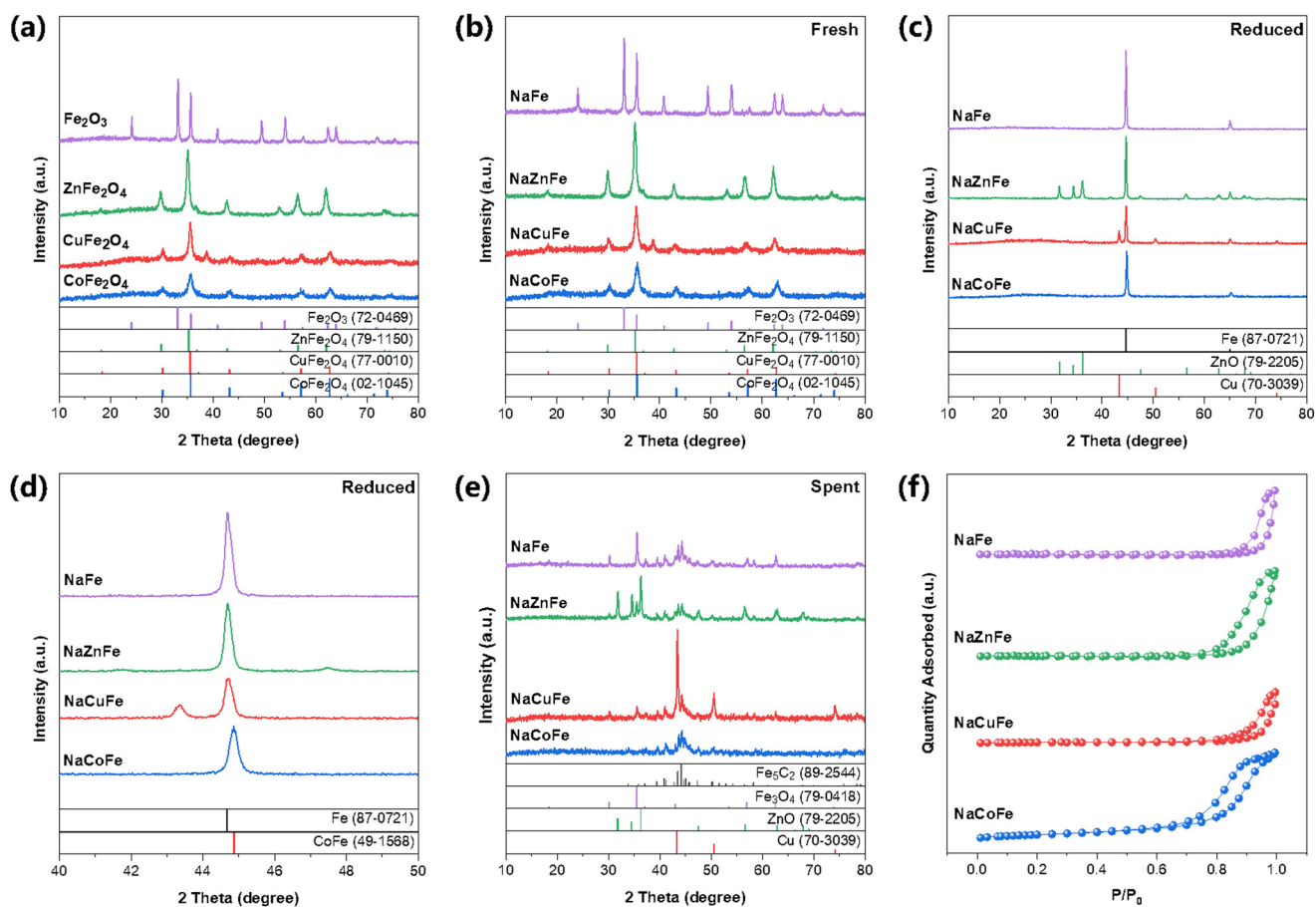


Fig. 2 XRD patterns of the Fe-based catalysts. (a) MFe_2O_4 ; (b) after calcination; (c and d) after H_2 reduction; (e) after reaction. (f) N_2 adsorption-desorption isotherms of fresh catalysts.



The XRD patterns (Fig. 2a) confirm the successful synthesis of spinel structure (MFe_2O_4). The XRD analysis of fresh catalyst (Fig. 2b) shows that the spinel structure is still retained after sodium modification. The absence of discrete diffraction peaks relevant to Na_2O or MO_x ($M = Zn, Cu, \text{ or } Co$) indicates that Na species are present in low concentration and are highly dispersed within the MFe_2O_4 bulk matrix. Using the Scherrer equation, we calculated the average crystallite size of a series of catalysts based on the diffraction peak position and half-width of Fe_2O_3 (110) and MFe_2O_4 (311). As shown in Table 1, compared to NaFe, the average crystallite size of NaMFe is significantly reduced, with NaCoFe catalyst having the smallest particle size of 7.8 nm, facilitating the formation of more active sites. After H_2 reduction (Fig. 2c), XRD patterns for NaFe catalyst show a predominance of metallic iron (Fe^0) peaks. For the reduced NaZnFe catalyst, the diffraction peaks belonging to $ZnFe_2O_4$ were negligible, whereas those corresponding to α -Fe (PDF#87-0721) and ZnO (PDF#79-2205) were clearly observable. In addition to the presence of α -Fe, the reduced NaCuFe was also found to contain metallic Cu, as evidenced by the peaks located at 43.3° and 50.4° (PDF#70-3039). It is worth noting that $CoFe_2O_4$ in NaCoFe catalyst is converted into CoFe alloy (PDF#49-1568) after reduction (Fig. 2d), which is much easier to be carburized than monometallic Fe or Co.²¹ Upon reaction (Fig. 2e), the spent sample was mainly composed of mainly Fe_3O_4 and Fe_5C_2 , which is considered as the active phase for RWGS and subsequent FT reaction. The ZnO phase was still visible in the spent NaZnFe catalyst, which has been reported to promote RWGS reaction and enhance stability.¹⁴ In the case of the spent NaCuFe catalyst, the Cu remained in metallic form, and Cu- Fe_5C_2 interface generally considered as the active site for CO_2 hydrogenation to alcohol species. It is noteworthy that the diffractions related to Fe_3O_4 for spent NaCoFe catalyst are weaker than those for other spent catalysts, indicating that the CoFe alloy phase is more prone to carbonization rather than oxidation during CO_2 hydrogenation.

SEM images and the corresponding elemental mapping images of the fresh catalysts are shown in Fig. S6 and S7.† These images reveal that Zn (Cu, Co), Fe, and O are uniformly dispersed across the catalysts, while Na is scarcely observed due to its low concentration. Notably, the Na element in NaZnFe is detectable, which may be due to the aggregation of Na and Zn.^{14,21,22} The N_2 adsorption-desorption isotherms of

all catalysts exhibit a IV-type isotherm, indicating a characteristic mesoporous structure (Fig. 2f). The formation of spinel structure clearly contributes to an increase in specific surface area (Table 1). Notably, the specific surface area increases significantly from $7.4 \text{ m}^2 \text{ g}^{-1}$ to $55.3 \text{ m}^2 \text{ g}^{-1}$ for the NaCoFe catalyst. Consequently, catalysts with larger specific surface areas are likely to demonstrate improved catalytic performance.

To elucidate specific active sites of spent catalyst, we employed TEM characterizations. TEM images of the spent NaCoFe catalyst (Fig. 3a) show that the catalyst structure consists of numerous nanoparticles with different particle sizes by stacking, which contributes to the formation of abundant mesopores. According to the uniform distribution of three metal elements in the spent NaCoFe catalyst as reflected from the element mapping of their scanning transmission electron microscopy (STEM) images (Fig. 3b), the Co and Fe species are observed to be in close proximity to each other, indicated by the presence of Fe in nearly all areas where Co was detected. As shown in Fig. S9,† Cu and Fe are uniformly distributed in the spent NaCuFe catalyst. However, for the spent NaZnFe catalysts, Zn and Na are predominantly distributed in regions complementary to those of Fe, suggesting a phase separation (Fig. S10†). The above results indicate that Co and Cu are beneficial for the dispersion of active metals. Furthermore, high-resolution transmission electron microscopy (HRTEM) was used to characterize the catalysts after the reaction (Fig. 3c). The lattice spacing of 0.213, 0.208, and 0.205 nm are observed in the spent NaCoFe catalyst, corresponding to Co_2C (111), Fe_5C_2 (021), and Fe_5C_2 (510) species, respectively. It is important to note that no obvious diffraction peaks of Co_2C were observed in the XRD spectrum, indicating that Co_2C is well dispersed and has a small particle size. It has been reported that small Co_2C nanoparticles with the Co_2C (111) surface exposed, favor methane selectivity,²³ consistent with our activity testing experimental observations (Fig. 1a). These results suggested that the presence of CoFe alloy phase promotes the formation of Fe_5C_2 and Co_2C during CO_2 hydrogenation process. Notably, all four catalysts exhibited a core-shell structure after the reaction, which can be attributed to carbon deposition on the surface of Fe_5C_2 particles.^{24,25} The two peaks at 1364 cm^{-1} and 1585 cm^{-1} in Raman spectra also confirmed the existence of carbon deposition (Fig. S11†).¹⁴

Table 1 Physical and chemical properties of the Fe-based catalysts

Catalysts	S_{BET}^a ($\text{m}^2 \text{ g}^{-1}$)	V^b ($\text{cm}^3 \text{ g}^{-1}$)	D^c (nm)	d_{fresh}^d (nm)	Na ^e (wt%)	$A_{CO_2}^f$ ($\times 10^{-8}$ a.u.)	$A_{H_2}^g$ ($\times 10^{-7}$ a.u.)	$A_{C_2H_4}^h$ ($\times 10^{-6}$ a.u.)
NaFe	7.4	0.15	28.8	43.1	1.9	17.7	3.9	4.2
NaZnFe	15.6	0.21	17.4	13.4	2.1	11.8	3.6	2.4
NaCuFe	10.5	0.13	27.7	11.7	2.0	10.4	4.3	2.2
NaCoFe	55.3	0.22	11.1	7.8	1.9	10.7	4.8	1.5

^a BET surface area calculated by the BET method. ^b BJH Desorption cumulative volume of pores. ^c BJH Desorption average pore width ($4V/S_{BET}$). ^d Calculated by Scherrer equation. ^e Detected by ICP-AES. ^f Desorption peak area of CO_2 in CO_2 -TPD. ^g Desorption peak area of H_2 in H_2 -TPD. ^h Desorption peak area of C_2H_4 in C_2H_4 -TPD.



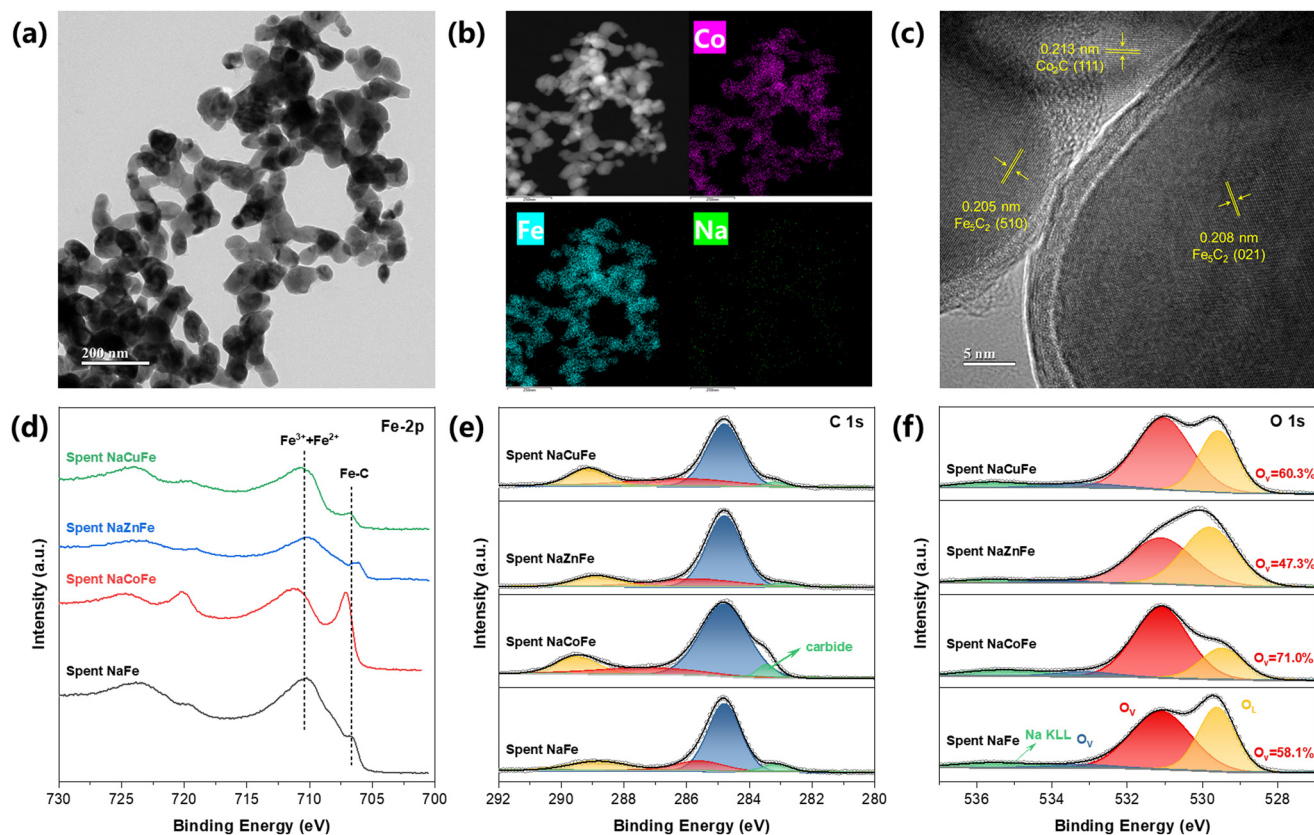


Fig. 3 (a) TEM images; (b) STEM images with corresponding elemental mapping of Co, Fe, Na and (c) HRTEM images of the spent NaCoFe sample. (d) Fe 2p; (e) C 1s and (f) O 1s XPS spectra of the spent Fe-based catalysts.

Chemical state and surface analysis of Fe-based catalysts

XPS analysis was performed on the spent samples to determine the chemical state of surface and surface iron carbide. For Fe 2p spectra (Fig. 3d), the spent samples show two broad peak centers, one near 710.5 eV and the other around 724.0 eV, representing Fe 2p_{3/2} and Fe 2p_{1/2} spin-orbit, respectively.²⁶ The peak centered around 710.5 eV also suggests that Fe³⁺ and Fe²⁺ species are the predominant components present on the surfaces of these spent catalysts.²⁷ The peak centered at 706.6 eV can be assigned to the Fe–C of the Fe₅C₂ phase.²⁶ Compared to the spent NaFe and NaCuFe, the lowered binding energy of iron carbide species in the spent NaZnFe is due to the electron interactions between Zn and iron species. Notably, an emerging component at 707.0 eV and 720.1 eV is identified in the spent NaCoFe catalyst, corresponding to the alloy carbide phase formed during the reaction.^{15,28} The increased intensity of the Fe₅C₂ peak in the spent NaCoFe indicates further progress in surface Fe species carburization, facilitated by the CoFe alloy. C 1s XPS spectra for spent catalysts (Fig. 3e) display four peaks corresponding to C=O, C–O, C=C, and carbides,²¹ respectively. The abundant iron carbide in the spent NaCoFe is further confirmed by the C 1s spectra, which show a prominent carbide feature at 283.4 eV.²⁹ The O 1s spectrum (Fig. 3f) can be deconvoluted into

peaks corresponding to adsorbed oxygen species (O_A) at 533.0 eV, oxygen vacancy (O_V) at 531.0 eV and oxygen lattice (O_L) at 529.5 eV.³⁰ The relative contents of oxygen vacancies among the three oxygen species increase in the order of NaZnFe (47.3%) < NaFe (58.1%) < NaCuFe (60.3%) < NaCoFe (71.0%). This indicates that the intensity of oxygen vacancy peaks is highest in the NaCoFe catalyst. It has been reported that catalysts containing spinel structures can exhibit high catalytic performance for light olefins through oxygen vacancies.³¹ The surface of NaCoFe catalyst has a higher proportion of oxygen vacancy concentration, which is favorable for catalytic performance.

Reduction and adsorption behavior of Fe-based catalysts

H₂-TPR measurements were used to study the promoting effect of transition metals on the catalysts reduction behaviors. As shown in Fig. 4a, the unpromoted NaFe catalyst displays three distinguishable reduction peaks, which reflects the stepwise nature of the reduction of Fe₂O₃ to metallic Fe. Specifically, the first H₂ consumption peak at 431 °C corresponds to the reduction of Fe₂O₃ to Fe₃O₄, while the peak around 560 °C and 770 °C are ascribed to the reductions of Fe₃O₄ to FeO and FeO to metallic Fe, respectively.^{32,33} The addition of Zn or Co enhances the reducibility of iron oxide species within the ferrite spinel



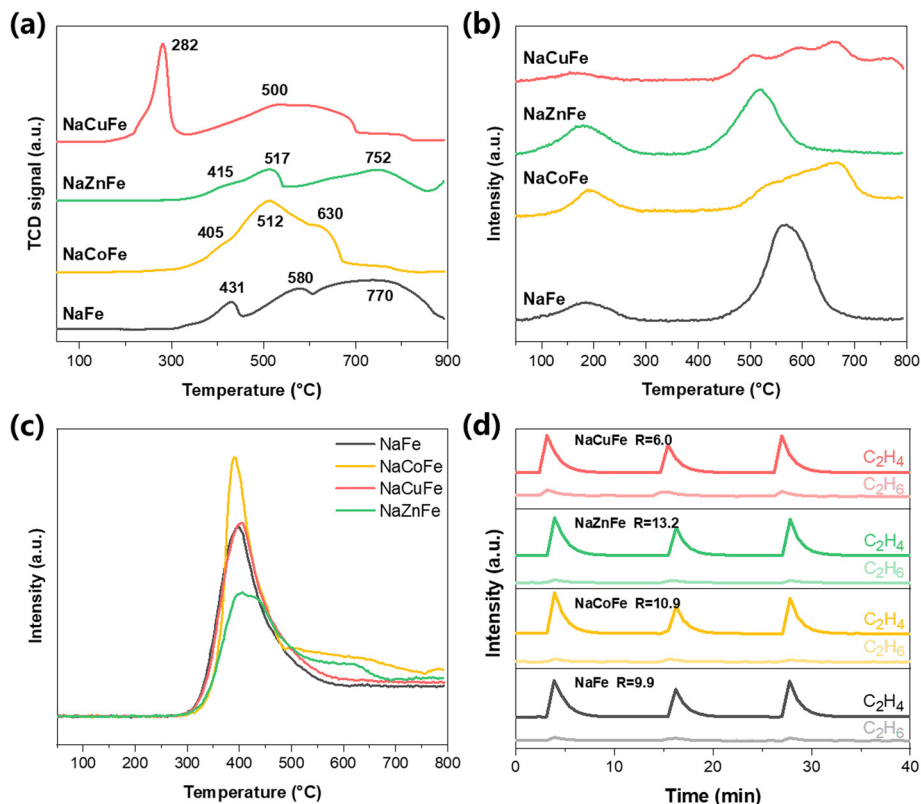


Fig. 4 (a) H₂-TPR; (b) CO₂-TPD; (c) H₂-TPD and (d) C₂H₄-PTH profiles of the Fe-based catalysts.

structure. For NaZnFe, the reduction process mirrors that of NaFe, but the peaks shift slightly to lower temperatures due to the formation of small ZnO clusters during synthesis, which further improves the dispersion of the Fe phase and the reduction behavior of the iron catalyst.³⁴ The reduction peaks of NaCoFe also shift towards lower temperatures, but a strong peak is clearly observed at 512 °C, which is due to the overlap between the reduction of CoO to metal Co and the reduction of Fe₃O₄.³⁵ For NaCuFe, two distinct reduction peaks are observed. The first peak at low temperature (<300 °C) corresponds to the reduction of CuO to Cu and Fe₂O₃ to Fe₃O₄, while the broad peak (>400 °C) is ascribed to subsequent conversion of Fe₃O₄. The shift to lower temperature (or increased reducibility of the catalyst) is likely linked to the H₂-activation of Cu site *via* H₂-spillover. The dissociation of hydrogen molecules on the Cu site is much easier than on the iron site, and the dissociated H can overflow from Cu and adsorb onto surrounding iron species, promoting the reduction of the catalyst.^{36,37}

The effects of transition metals on the spent catalysts were examined using the CO₂-TPD measurements, as the CO₂ adsorption capacity of Fe-based catalysts is crucial for their performance in CO₂ hydrogenation reactions. The adsorption of CO₂ by catalysts can be divided into three intensities: weak adsorption at 100–300 °C; medium adsorption at 300–500 °C and strong adsorption at 500–800 °C. As shown in Fig. 4b, all TPD profiles exhibit a broad and low peak at 180 °C, which is indicative of the

desorption of CO₂ molecules weakly adsorbed within the bulk phase. The main desorption peak located at 500–800 °C corresponds to the desorption of CO₂ that strongly interacts with the surface basic sites.³⁸ Obviously, the four catalysts have different strong adsorption sites for CO₂, and we calculated the desorption peak area in the high-temperature region, as listed in Table 1. Although the CO₂ adsorption capacity decreases with the formation of spinel structure, the conversion rate of CO₂ has not decreased (Fig. 1a). This suggests that CO₂ conversion is not solely dependent on its adsorption capacity.

It is well known that the H₂ adsorbed onto the catalyst surface enhances the RWGS reaction and facilitates subsequent FT synthesis. To investigate the activation of H₂ on the catalyst, H₂-TPD experiments were conducted, with the results presented in Fig. 4c and Table 1. It is found that the desorption of H₂ from the spent NaCoFe catalyst and NaCuFe catalyst is higher than that of the spent NaFe catalyst, whereas Zn reduces the adsorption capacity of H₂. This suggests that CoFe₂O₄ and Cu₂FeO₄ effectively trigger H₂ spillover, resulting in improved H₂ desorption on the NaCoFe and NaCuFe catalysts. Furthermore, the largest amount of H₂ desorption is attributed to the highest iron carbide content formed on the used NaCoFe catalyst,³⁹ as corroborated by XPS results. These experimental results indicate that the CO₂ conversion rate of different transition metal spinel catalysts is largely constrained by their hydrogenation ability.



Reabsorption reaction behavior of olefins

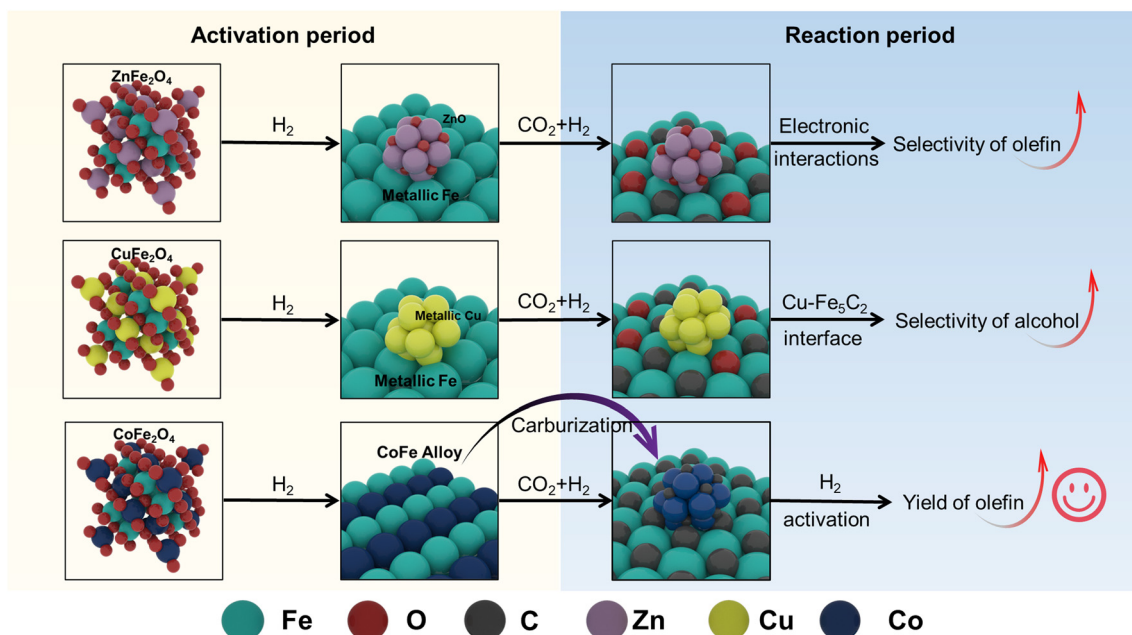
As a product of FTS reaction, olefins adsorb on the catalyst surface and can re-enter the reaction. Although the hydrogenation ability of the catalyst can promote the improvement of its CO₂ conversion rate, excessive hydrogenation ability may also lead to secondary hydrogenation of olefin products on the catalyst surface to form paraffins. Therefore, understanding whether olefins preferentially undergo desorption or hydrogenation on the catalyst is crucial. For this purpose, temperature-programmed desorption of C₂H₄ measurements (C₂H₄-TPD) were performed on the spent catalysts. As shown in Fig. S12† and Table 1, the introduction of transition metals reduces the adsorption strength of the catalyst for C₂H₄, which may facilitate the desorption of olefin products on the catalyst surface.

To further elucidate the impact of transition metals on the secondary hydrogenation capacity of olefins under the reaction conditions, pulse transient hydrogenation (PTH) experiments were employed using C₂H₄ as the study gas. Before conducting the measurements, the spent catalysts were *in situ* reduced. Fig. 4d reveals that each catalyst possesses the ability to convert olefins into paraffins under a continuous stream of H₂/Ar. The *R*-value reflects the ability of olefins to undergo secondary hydrogenation on the catalyst surface, with lower *R* values indicating easier conversion of olefins to alkanes. The ratio of C₂H₄/C₂H₆ peak area increases in the order of NaCuFe (6.0) < NaFe (9.9) < NaCoFe (10.9) < NaZnFe (13.2). The highest *R* value of NaZnFe catalyst may be due to the electron-donating effect from Zn to Fe₅C₂,⁴⁰ as confirmed by XPS results (Fig. 4a). According to reports, the presence of Na can hinder the secondary

hydrogenation of olefins by reducing the adsorption of olefins on the surface of iron catalysts.¹⁹ In this work, the sodium content of the fresh catalysts and spent catalysts is around 2 wt%, as evidenced by ICP-AES analysis (Table 1). This finding suggests that the secondary hydrogenation of olefins to paraffins is suppressed with the addition of Zn or Co, whereas the Cu promoter enhances the capability of secondary hydrogenation of olefins leading to lower selectivity. It is worth noting that in the catalyst activity test, we did not observe a significant increase in the olefin selectivity of NaZnFe and NaCoFe, which may be due to their excessive methane products.

Discussion on the role of transition metals in spinel

Based on our experimental findings, the precursors of spinel structure increase the specific surface area and reduce particle size of the resulting catalysts. Furthermore, these precursors facilitate improved reducibility while promoting dispersion of both transition metal species and active iron sites. Then we propose the following structural evolution for various Na-decorated binary spinel ferrite catalysts (Scheme 1). ZnFe₂O₄ effectively promotes the reduction of Fe species, transforming into metallic iron and ZnO upon H₂ activation. The electronic interactions between ZnO and Fe species in the spent NaZnFe catalyst inhibit secondary olefins hydrogenation, which is beneficial for enhancing olefin selectivity. However, in this work, Zn additive seems to suppress the catalytic performance. This may be due to its weaker dissociation activation ability towards the reactant hydrogen (H₂-TPD) and the phase segregation of Zn and Fe (STEM). Conversely, CuFe₂O₄ significantly enhances catalyst reduction through H₂-spillover at the Cu site. However, the



Scheme 1 The structure evolution of different binary spinel ferrite catalysts during the activation and reaction period.



strong hydrogenation capability and the Cu-Fe₅C₂ interface in the spent NaCuFe catalyst lead to increased alcohol production, which reduces olefin yield. CoFe₂O₄ facilitates the reduction of Co and Fe species, resulting in the formation of CoFe alloy. This alloy readily carbides into Fe₅C₂ and Co₂C during the reaction, and its robust hydrogen activation and dissociation abilities further boost the CO₂ conversion rate. Moreover, Co species in CoFe₂O₄, known for their activity in CO₂/CO hydrogenation, accelerate the consumption of intermediates, thereby further increasing CO₂ conversion. As a result, the NaCoFe catalyst demonstrates the highest CO₂ hydrogenation activity and olefin yield.

Conclusion

In summary, we investigated the effects of different transition metals on the physicochemical properties and catalytic performance of spinel structures during the hydrogenation of CO₂. ZnFe₂O₄ and CuFe₂O₄ were found to facilitate reduction but decrease olefin yield, whereas CoFe₂O₄ significantly enhanced both CO₂ conversion and olefin yield. Characterization techniques such as physical adsorption, XRD, and chemical adsorption revealed that the CoFe alloy promotes the formation of the carbide phase and enhances the activation and dissociation of hydrogen. This work not only provides new insights into the role of spinel structures in promoting catalytic reactions but also offers fresh perspectives for designing Fe-based catalysts for CO₂ hydrogenation.

Data availability

The data supporting this article have been included as part of the ESI.†

Author contributions

The manuscript was written through the contributions of all authors. All authors have approved the final version of the manuscript.

Conflicts of interest

The authors declare no competing financial interest.

Acknowledgements

The support for this project from the Department of Applied Biology and Chemical Technology at the Hong Kong Polytechnic University (PolyU P0049034) is gratefully acknowledged.

Notes and references

- G. A. Meehl, W. M. Washington, W. D. Collins, J. M. Arblaster, A. X. Hu, L. E. Buja, W. G. Strand and H. Y. Teng, *Science*, 2005, **307**, 1769–1772.
- A. Kätelhön, R. Meys, S. Deutz, S. Suh and A. Bardow, *Proc. Natl. Acad. Sci. U. S. A.*, 2019, **116**, 11187–11194.
- E. V. Kondratenko, G. Mul, J. Baltrusaitis, G. O. Larrazábal and J. Pérez-Ramírez, *Energy Environ. Sci.*, 2013, **6**, 3112.
- R.-P. Ye, J. Ding, W. Gong, M. D. Argyle, Q. Zhong, Y. Wang, C. K. Russell, Z. Xu, A. G. Russell, Q. Li, M. Fan and Y.-G. Yao, *Nat. Commun.*, 2019, **10**, 5698.
- X. Jiang, X. Nie, X. Guo, C. Song and J. G. Chen, *Chem. Rev.*, 2020, **120**, 7984–8034.
- Z. Ma and M. D. Porosoff, *ACS Catal.*, 2019, **9**, 2639–2656.
- G. Tian, X. Liang, H. Xiong, C. Zhang and F. Wei, *EES Catal.*, 2023, **1**, 677–686.
- P. Gao, L. Zhang, S. Li, Z. Zhou and Y. Sun, *ACS Cent. Sci.*, 2020, **6**, 1657–1670.
- D. Xu, Y. Wang, M. Ding, X. Hong, G. Liu and S. C. E. Tsang, *Chem*, 2021, **7**, 849–881.
- D. Goud, R. Gupta, R. Maligal-Ganesh and S. C. Peter, *ACS Catal.*, 2020, **10**, 14258–14282.
- Z. Zhang, G. Huang, X. Tang, H. Yin, J. Kang, Q. Zhang and Y. Wang, *Fuel*, 2022, **309**, 122105.
- J. Jiang, C. Wen, Z. Tian, Y. Wang, Y. Zhai, L. Chen, Y. Li, Q. Liu, C. Wang and L. Ma, *Ind. Eng. Chem. Res.*, 2020, **59**, 2155–2162.
- J. I. Orege, G. A. Kifle, Y. Yu, J. Wei, Q. Ge and J. Sun, *Matter*, 2023, **6**, 1404–1434.
- C. Zhang, C. Cao, Y. Zhang, X. Liu, J. Xu, M. Zhu, W. Tu and Y.-F. Han, *ACS Catal.*, 2021, **11**, 2121–2133.
- K. Y. Kim, H. Lee, W. Y. Noh, J. Shin, S. J. Han, S. K. Kim, K. An and J. S. Lee, *ACS Catal.*, 2020, **10**, 8660–8671.
- Y. H. Choi, Y. J. Jang, H. Park, W. Y. Kim, Y. H. Lee, S. H. Choi and J. S. Lee, *Appl. Catal., B*, 2017, **202**, 605–610.
- D. Xu, M. Ding, X. Hong, G. Liu and S. C. E. Tsang, *ACS Catal.*, 2020, **10**, 5250–5260.
- T. Liu, D. Xu, M. Song, X. Hong and G. Liu, *ACS Catal.*, 2023, **13**, 4667–4674.
- H. Yang, Y. Dang, X. Cui, X. Bu, J. Li, S. Li, Y. Sun and P. Gao, *Appl. Catal., B*, 2023, **321**, 122050.
- H. Yang, Z. Wei, J. Zhang, Y. Dang, S. Li, X. Bu, Z. Zhou, C. Gong, H. Wang, J. Li, Y. Liu, Y. Yang, T. Xiao, C. Liu, Y. Sun and P. Gao, *Chem*, 2024, **10**, 2245–2265.
- Q. Xu, X. Xu, G. Fan, L. Yang and F. Li, *J. Catal.*, 2021, **400**, 355–366.
- P. Zhai, C. Xu, R. Gao, X. Liu, M. Li, W. Li, X. Fu, C. Jia, J. Xie, M. Zhao, X. Wang, Y. Li, Q. Zhang, X. Wen and D. Ma, *Angew. Chem., Int. Ed.*, 2016, **55**, 9902–9907.
- Y. Dai, Y. Zhao, T. Lin, S. Li, F. Yu, Y. An, X. Wang, K. Xiao, F. Sun, Z. Jiang, Y. Lu, H. Wang, L. Zhong and Y. Sun, *ACS Catal.*, 2018, **9**, 798–809.
- Y. Zhang, C. Cao, C. Zhang, Z. Zhang, X. Liu, Z. Yang, M. Zhu, B. Meng, J. Xu and Y. Han, *J. Catal.*, 2019, **378**, 51–62.
- J. Xu and C. H. Bartholomew, *J. Phys. Chem. B*, 2005, **109**, 2392–2403.
- J. I. Orege, J. Wei, Y. Han, M. Yang, X. Sun, J. Zhang, C. C. Amoo, Q. Ge and J. Sun, *Appl. Catal., B*, 2022, **316**, 121640.
- Y. Xu, P. Zhai, Y. Deng, J. Xie, X. Liu, S. Wang and D. Ma, *Angew. Chem., Int. Ed.*, 2020, **59**, 21736–21744.



- 28 Y. Liu, Q. Cheng, S. Lyu, X. Li, S. Song, T. Ding, Y. Tian and X. Li, *Chem. Eng. J.*, 2024, **494**, 152936.
- 29 P. Du, R. Qi, Y. Zhang, Q. Gu, X. Xu, Y. Tan, X. Liu, A. Wang, B. Zhu, B. Yang and T. Zhang, *Chem*, 2022, **8**, 3252–3262.
- 30 M. K. Khan, P. Butolia, H. Jo, M. Irshad, D. Han, K.-W. Nam and J. Kim, *ACS Catal.*, 2020, **10**, 10325–10338.
- 31 J. Ding, L. Huang, W. Gong, M. Fan, Q. Zhong, A. G. Russell, H. Gu, H. Zhang, Y. Zhang and R.-p. Ye, *J. Catal.*, 2019, **377**, 224–232.
- 32 S. Ma, M. Li, G. Wang, L. Zhang, S. Chen, Z. Sun, J. Hu, M. Zhu and W. Xiang, *Chem. Eng. J.*, 2018, **346**, 712–725.
- 33 Y. Yang, W. Qian, H. Zhang, Z. Han, H. Ma, Q. Sun and W. Ying, *Catal. Sci. Technol.*, 2022, **12**, 4624–4636.
- 34 J. Zhang, S. Lu, X. Su, S. Fan, Q. Ma and T. Zhao, *J. CO₂ Util.*, 2015, **12**, 95–100.
- 35 C. Yang, S. Liu, Y. Wang, J. Song, G. Wang, S. Wang, Z.-J. Zhao, R. Mu and J. Gong, *Angew. Chem., Int. Ed.*, 2019, **58**, 11242–11247.
- 36 Z. H. Chonco, L. Lodya, M. Claeys and E. van Steen, *J. Catal.*, 2013, **308**, 363–373.
- 37 N. Chaipraditgul, T. Numpilai, C. Kui Cheng, N. Siri-Nguan, T. Sornchamni, C. Wattanakit, J. Limtrakul and T. Witoon, *Fuel*, 2021, **283**, 119248.
- 38 C. Zhang, Y. Yang, B. Teng, T. Li, H. Zheng, H. Xiang and Y. Li, *J. Catal.*, 2006, **237**, 405–415.
- 39 Q. Yang, V. A. Kondratenko, S. A. Petrov, D. E. Doronkin, E. Saraci, H. Lund, A. Arinchtin, R. Kraehnert, A. S. Skrypnik, A. A. Matvienko and E. V. Kondratenko, *Angew. Chem., Int. Ed.*, 2022, **61**, e202116517.
- 40 C. Zhang, M. Xu, Z. Yang, M. Zhu, J. Gao and Y.-F. Han, *Appl. Catal., B*, 2021, **295**, 120287.

